V&V for turbulent mixing in the intermediate asymptotic regime

H. Zhang, T. Kaman, D. She, B. Cheng, J. Glimm, and D. H. Sharp

Abstract: Turbulent fluid flow interacts nonlinearly with a number of processes, including reactive flow (chemistry), radiation, and the transport of particles embedded in the flow. Subgrid scale modeling of these nonlinear processes is a major challenge to computational science. To this end, turbulent mixing of dissimilar fluids is a driver. Here we study validation issues for a class of turbulent mixing simulations. In previous work, we have obtained agreement between simulation and experiment. The present paper addresses a remaining issue, the role of meniscus related boundary effects for immiscible fluids in the validation process.

Validation and even verification has been controversial for turbulent mixing flows, as commonly used numerical models are diffusive and the resulting numerical diffusion modifies the parameters of the problem and its solution. Numerical diffusion of concentration and temperature is well documented in the scientific literature for Eulerian simulations. Lagrangian simulations, which might appear to avoid this problem, are subject to mesh tangling, ensuing regridding and use of Arbitrary Lagrangian Eulerian codes to substitute for a pure Lagrangian algorithm. In practice, Lagrangian methods are potentially subject to the same numerical diffusion issues when used to study complex interface instabilities.

Keywords: Rayleigh-Taylor instability, large eddy simulation, turbulent mixing.

1. Introduction

1.1. Problem formulation

The nonlinear coupling of turbulent flow to other processes, such as reactive flow (chemistry), radiation and particle transport is a major challenge for computational fluid dynamics. The turbulent mixing of dissimilar fluids is at

the heart of the problem. Turbulent mixing, considered beyond the focus of this article, is surveyed in the articles [57, 58]. Here we address verification and validation (V&V) for acceleration driven turbulent mixing flows, based on the experimental data from [49]. We emphasize regimes for which V&V is most problematic. We consider the intermediate asymptotic regime, meaning the transition from small initial data to sustained Rayleigh-Taylor (RT) and Richtmyer-Meshkov (RM) growth, and in this regime, we emphasize low diffusion and rapid acceleration physics. Current concerns regarding early time cold fuel and the ablation front surface instability effects in Inertial Confinement Fusion (ICF) capsules suggest that there is a present value to the resolution of this controversy. The possibility of reaching National Ignition Facility (NIF) ignition should be determined by 2020 [25]. Hydrodynamic mixing during implosion is one of the important issues. Correctly calculating the ablator-fuel mixing and cold-hot fuel mixing is important for improving future ignition capsule designs [6, 28]. Current numerical diffusion dominated algorithms may well under estimate the RT and RM generated mix and over estimate the capsule performance. Therefore, resolving this V&V controversy may help to improve ignition studies.

Our main conclusion is:

> The leading order time asymptotics $\alpha_2 \sim 0.06 \pm 0.01$ for Rayleigh-Taylor mixing observed experimentally [49] is not contaminated appreciably by long wave noise in the initial conditions.
> In support of this claim, we offer three secondary conclusions:

a) Adherence to standards of V&V is a more reliable indicator of scientific truth than is a scientific consensus.

b) Multiple independent simulations (free from artifacts of numerical diffusion) and a quantitative theory from multiple independent groups support standards of V&V for our central claim.

c) The role of the meniscus in immiscible experiments is analyzed in detail here, and found to contribute to the growth at a next to leading order in the time asymptotics, but leaves the α_2 leading order asymptotics largely unchanged. Thereby, our central claim, as analyzed in [18], is confirmed.

The next to leading order term in the late time asymptotics is an important technical issue and may be significant within an ICF context. ICF occurs on a highly compressed time scale, making the late time leading order asymptotics of the mixing dynamics an incomplete characterization of mix. In view of the variation in definitions of the leading order asymptotics, comparison of

next to leading order corrections between different working groups is meaningless. Here we adopt a different point of view. We apply a consistent set of definitions to both theory and experiment, for the leading order asymptotics and for the delay. As a validation test, we compare simulation to experiment within these consistent definitions.

Most algorithms used for turbulent mix are numerically diffusive, and the resulting concentration and thermal diffusion modify the effective parameters governing the solution. In effect, numerical artifacts accomplish a modification of the physics, so that the common numerical solutions are correct solutions to a problem with modified physics parameters. With these algorithms, validation is rarely attempted in a low diffusion, rapid acceleration rate context and even verification succeeds only at a qualitative level and can fail when assessed quantitatively, because the numerical artifacts and the resulting numerical adjustment of the (physics) parameters in the problem actually solved vary from one code to another, making cross code comparisons inconclusive. In contrast, the Front Tracking algorithms of the authors have achieved excellent verification and validation results [26, 18] for low diffusion, strong acceleration data [49].

Two objections to this verification and validation success have been raised. The primary objection was that long wave length perturbations present in the initial data could change the results and had not been included in the analysis. The problem was resolved in [18], where it was shown that long wave length perturbations were indeed present in the experiments of [49]. However, due to the slow growth of the long wave length perturbations, their contribution to the overall instability growth rate was limited to $\pm 5\%$. The second objection was that the immiscible fluid meniscus at the container wall initial interface gave rise to edge effects in the (face-on camera view) observed instability growth rates which had not been analyzed. As the simulations studied in [18] were immiscible, and thus do possess a meniscus in their initial interface, the second objection questions the resolution of the first objection. The second objection (and thus also the first) is addressed in the present paper.

Acceleration driven fluid mixing is characterized by an acceleration time scale, so that the asymptotic penetration distance h_2 of the light fluid (bubbles) into the heavy fluid is characterized by the formula $h_i = \alpha_i A g t^2$, where the Atwood number $A = (\rho_1 - \rho_2)/(\rho_1 + \rho_2)$ is a buoyancy correction to the accelerating force g and ρ_i denotes the fluid densities, $i = 1$ being the heavy fluid and $i = 2$ the light. The complementary penetration of the heavy fluid into the light is called a spike. α_i is a dimensionless coefficient that characterizes the leading order large time asymptotics for the mixing process. There may be a delay before this terminal acceleration mixing rate is achieved, and

the formula

$$(1) \qquad h_i = \alpha_i Ag(t - t_{i,a})^2, \qquad t > t_{i,a}$$

allows for a delay or transition time $t_{i,a}$ to full acceleration. The restriction $t > t_{i,a}$ reflects the fact that the transition period has more complex dynamics and is not modeled by (1). The idea of a delay has been introduced in a number of studies, including ones by the authors, but its systematic numerical study to characterize the next to leading order asymptotics at the level conducted here covers new ground.

The main new result of this paper states that the meniscus effect in experiments with immiscible fluids has a strong influence on the delay but leaves the growth rate α_2 unchanged. This result removes the meniscus related uncertainties in the characterization of α_2. The bubbles in the immiscible experiments share a common growth rate α_2, whether they are bulk bubbles located in the interior of the fluid or edge bubbles, located at the edge of the container, with the edge bubbles directly observed. The only difference between the two cases is in the delay. The actual delay is imperfectly observed, and for three experiments only. It is also inferred from 2D simulation studies, validated by experimental data. We further confirm this main assertion by displaying a one parameter family of simulations modeling experiment 105 [49] and indexed by the delay. All members of the family share a common acceleration growth constant $\alpha_2 = \alpha_2^{105}$. In summary, the validity of the previous V&V analysis of the RT mixing growth rate α_2 for experiment 105 of ref. [49] with inclusion of experimentally determined long wave length perturbations from the initial data is confirmed.

It is convenient to measure delay in height units, as these are more consistently compared across experiments and combined from multiple sources. Thus we also define the delay $h_{i,a} = \text{sgn}(t_{i,a})\alpha_i g t_{i,a}^2$ measured in height units and representing the negative height axis intercept of the h_i vs. Agt^2 growth law. This reformulation of delay leads to the equation

$$(2) \qquad h_2 - h_{2,a} = \alpha_2 X ; \qquad X = Agt^2 .$$

We have $t_{i,a} > 0$ as a delay and with this sign convention, $h_{i,a} > 0$ is a delay also.

Physically, the steady increase in mixing rates (constant acceleration) is achieved by the interactions between adjacent bubbles and the continued increasing of the bubble widths (referred to as bubble merger) [8].

The experiments of ref. [49] feature a tank containing two fluids, with the light fluid on top, and which is accelerated rapidly downward (effectively

reversing the direction of gravity, so that the fluids are in an unstable configuration). The initial interface is nominally flat, other than its meniscus. For computational purposes, this nominally flat portion of the initial interface between the two fluids is modeled as a small amplitude perturbation formed from random Fourier modes, centered in a band about the maximally unstable wave length λ_m. We study vertical rig experiments 99, 103, 104, 105 and 114 of [49], namely all immiscible experiments of [49] having sufficient experimental data for our analysis. There are five tilted rig experiments 95, 96, 109, 110 and 115. Experiments 95, 96 and 109 have matched index of refraction and perhaps for this reason, edge effects are not visible. Experiment 110 has miscible liquid and not subject to the analysis of edge effects. Experiment 115 has visible edge spikes, but no visible bulk bubbles. In principle the methods of this paper would allow analysis of the edge spikes in experiment 115. As the experiments analyzed included both cases of visible bulk bubbles and an absence of visible bulk bubbles, we draw no conclusion from their absence in Exp. 115.

1.2. Delayed growth for the miscible experiment 112

The miscible experiment 112 has no meniscus and no edge effect. It satisfies formula (2) for the asymptotics of constant acceleration mixing to leading and next to leading order (i.e., delay). Experiment 112 has an $X = Agt^2$ intercept of 80 mm for its $h_{2,a}$ vs. X linear fit, thus a delay $h_2 = 80\alpha_2^{112} = 80 \times .052 = 4.16$ mm. The value $\alpha_2^{112} = 0.052$ is a correction [26] with permission of D. Youngs to the value from [49]. Experiment 112 has an initial diffusion layer of 3.5 mm, so that its dominant growing wave length should be comparable to the $\lambda_m = 4$ to 4.5 mm of the immiscible experiments. This fact suggests comparable frequencies for selection of noise levels dominant for instability initiation and explains the comparable acceleration growth rates and spike delays between these distinct immiscible and miscible experiments.

In spite of the comparable acceleration growth rates α_2 between 112 and the immiscible experiments, there is a striking difference in the delays between the miscible 112 (4 mm) and the delay (0 mm) of the observed edge bubbles of the immiscible experiments.

1.3. Edge effects

Our focus is on the meniscus induced edge effects and the modification to the steady acceleration asymptotics they produce. The study of spike edge effects leads to the dynamics of isolated 2D spikes for an initial time, until they

become unstable to 3D perturbations. The large time asymptotic dynamics during this period is a terminal velocity, with a penetration distance $h_i = Fr_i\sqrt{Ag\lambda}t$, with $i = 1$ for spikes. Here λ is the wave length of the isolated bubble or spike and Fr_i a 2D dimensionless Froude number characterizing a spike or bubble terminal velocity, neither well characterized for $i = 1$ and meniscus initial conditions. Thus we employ a simpler scaling analysis. We introduce the edge spike asymptotic scaling with the dimensionless velocity v^* and delay $h_{1,v}$ defined by the equations

(3) $$h_1 - h_{1,v} = v^*Y; \qquad Y = \sqrt{Ag}t \quad (mm) \ .$$

The meniscus is a spike of heavy fluid penetrating into the light fluid at the rim of the container, contributing to the light-heavy fluid interface initialization. Aside from corners of the experimental tank, the meniscus and the edge spike it generates are uniform and unperturbed by random surface perturbations for Plates 1-4 of Exp. 105, and for Plates 1-3 for the other experiments. As modeled by (3), i.e., while still 2D, the edge spikes are characterized by an asymptotic velocity $v*$ and a delay. The growth rate $v*$ of the edge bubble is sensitive to the meniscus contact angle, and using this fact, we set the contact angle to achieve identity of growth rates between simulation and experiment, as is defined by the spike amplitudes at the third and fourth plates. Determination of the contact angle from 2D simulations can be carried out for Exp. 105, but is approximate for the other experiments.

Edge spikes for Exp. 114 are shown in Fig. 1. A 2D simulation of an edge spike for Exp. 105 is shown in Fig. 2, left frame. The edge spike gives rise to a complementary edge bubble, also located along the container sides. We call these meniscus bubbles "m-bubbles", with the m referring to meniscus, to distinguish them from edge and bulk bubbles. See also Fig. 2, left frame. In contrast to the edge spike, this meniscus induced 2D edge m-bubble is not directly observable. The m-bubble amplitude is relatively insensitive to the choice of contact angle.

The bulk bubbles are visible through the edge bubbles, as shown in Fig. 3. The bulk of the fluid is subject to initial random surface perturbations and is unaffected by the meniscus initial perturbation. The random surface perturbations which initialize the bulk bubbles are modeled with modes in a band near the maximum unstable mode λ_m and with corrections for long wave length perturbations [18].

The bulk bubbles are visible for isolated periods, usually including the third plate, and more extensively for Exps. 103, 105 and 114. For these three experiments we compare the observed bulk bubble dynamics to the acceleration with delay formula (2). For experiment 114, the peak penetration of the
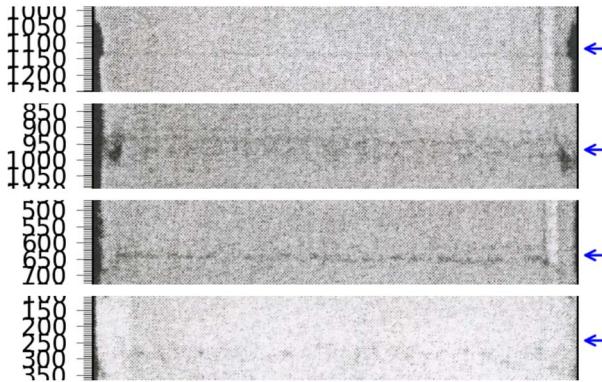
Figure 1: Enlarged slices from the experimental plates of [49], experiment 114. Plates 3 through 6 for edge spikes. The location of the edge spikes in each plate is indicated by the arrow on the left. It is only marginally visible even in this enlarged image. The scale on the left (units 10^{-1} mm from container top) was added for convenient reference. © British Crown Owned Copyright 2018/AWE.

bulk bubbles can be observed through the transparent edge bubbles for the entire experiment. See Fig. 3.

To better understand the steps which will be used to understand the unobserved m-bubble, we introduce the schematic diagram Fig. 4.

In Fig. (4), 0 is the initial interface position. G is the location of a pure α_2 growing interface at time t, which coincides with the edge bubble interface, reported from [49]. N is the average location of the edge bubble tips, as observed from the experimental plates of [49]. We apply Fourier analysis to the bubble tips, and recognize N as the $k = 0$ mode in this analysis. $G - N$ is the RMS sum of the nonzero Fourier modes. B is the time t location of the bulk bubble interface, which we seek to determine from our analysis, and for which limited observations are available from [49]. According to the combined effects analysis of Sec. 3.3, $N - B$ (in the Plate 3 analysis) is the m-bubble. We discuss in Sec. 3.1 a 2D simulation shown in Fig. 2 of the edge spike and its m-bubble to determine $N - B$ qualitatively. By subtraction, B is also determined qualitatively. We also express the splitting of B in terms of fractions, defining the fraction $f = B/N$ associated with the delay and the fraction $1 - f = (N - B)/N$, associated with the broad band random noise in the initial data. For Exp. 105, we find that f is near one, but due to limitations of the observed data, we cannot go beyond such a qualitative statement. The 2D simulation of the edge spike has an unknown contact angle
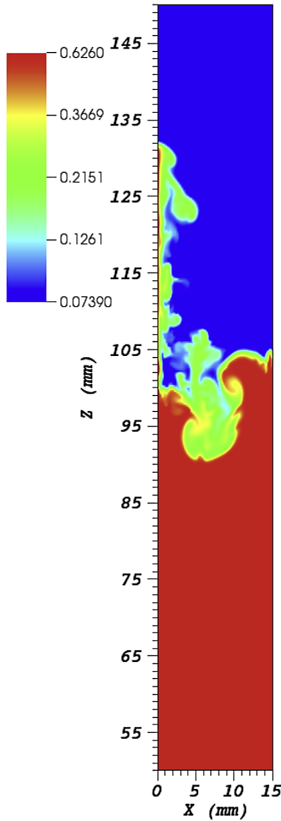
(a) The edge spike and the resulting m-bubble are shown in a density profile for Plate 3 of Exp. 105. The light fluid is shown in blue and the heavy fluid in red.
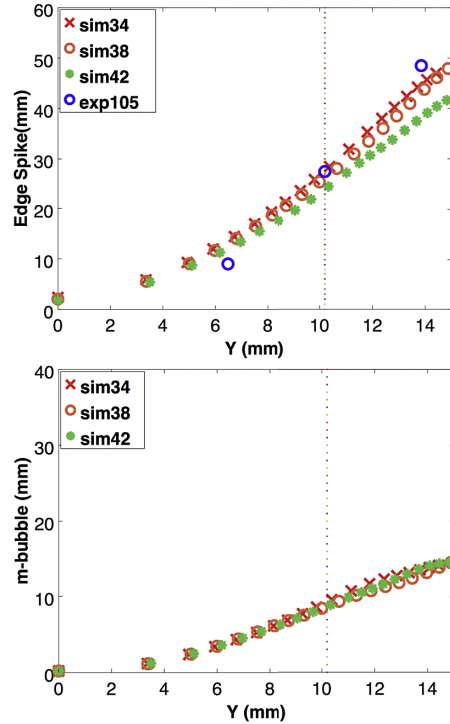
(b) Top: edge spikes height vs. scaled distance Y. Simulations for various contact angles and experimental data. From this data we select a contact angle (about 34°). Bottom: the m-bubble height vs. scaled distance Y. The 3rd plate ($Y = 10$) height is universal, independent of contact angle.

Figure 2: 2D simulation of meniscus effects for Exp. 105. Detailed values in comparison to experiment are qualitative only as discussed in the text. The resulting delay for the simulation of bulk bubbles, attributed to the m-bubble has a large fraction $f \sim 1$. See Fig. 8.

as input, so we use the edge spike data and the model (3) to adjust the contact angle and fit the observed slope $v*$ of the linear in t growth rate. This analysis is valid for experiment 105, and is approximate for the high Atwood number experiments, due to the presence of 3D perturbations in the edge spikes at Plate 4 in these cases.
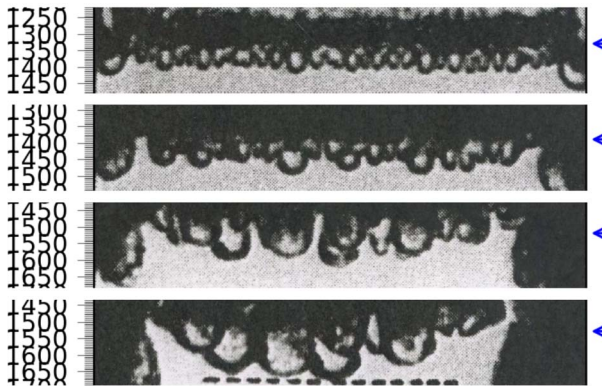
Figure 3: Enlarged slices from the experimental plates of [49], experiment 114. Plates 2 through 5 for bulk bubbles. The arrows on the right indicate the location of the bulk bubble interface. In the final frame, the dashed line is the 95% contour for the edge bubbles, as drawn in [49]. © British Crown Owned Copyright 2018/AWE.
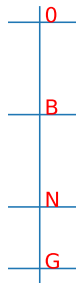

Figure 4: Schematic diagram of the principal variables discussed in this chapter. Item 0 is the initial interface position. G is the location of pure α_2 growth and also the location of the edge bubble interface as observed from [49]. B is the location of the bulk bubble interface and N is the mean bubble location for the edge bubbles. G and N are directly observed, while our analysis seeks to locate the imperfectly observed B.

Two classes of simulations are reported here. The 3D simulations use the compressible Front Tracking code, as is described in [18]. The 2D simulations of meniscus bubbles and spikes use an incompressible code based on a marker and cell (MAC) grid and the Immersed Boundary Method, as described in [59]. The solution algorithm uses portable, extensible toolkit for scientific

Table 1: Meniscus heights (mm) for selected contact angles, for 5 experiments

	90°	60°	45°	30°
Exp. 99	0.0	0.88417	1.53143	2.65251
Exp. 103	0.0	0.86667	1.5011	2.6000
Exp. 104	0.0	0.88676	1.53591	2.66027
Exp. 105	0.0	0.91824	1.59044	2.75472
Exp. 114	0.0	0.87754	1.51944	2.63262

computation (PETSc), a library of high performance preconditioners (hypre), and an algebraic multigrid preconditioner. These solutions use a 3D code, but operate in a 2D mode, with a narrow mesh in the wall parallel direction. The 2D character of the solution is imposed by an averaging step after every dynamic time step. Further solution details may be found in [52].

2. Meniscus theory

We review the standard theory of surface tension related boundary effects. The static meniscus height h, as a function of the distance x to the wall, is governed by the ordinary differential equation [30]

$$(4) \qquad \frac{d^2h}{dx^2} = \sqrt{\left(1 + \left(\frac{dh}{dx}\right)^2\right)^3 \frac{\rho g}{\sigma} h} \;,$$

where $\rho = \rho_1 - \rho_2$, g is the static acceleration and σ is the surface tension. This equation requires two boundary conditions. At the outer reaches of the meniscus, the fluid interface is asymptotically horizontal, giving one boundary condition. The second boundary condition occurs at the wall-fluid triple point, where the fluid-fluid interface meets the container wall. The angle of the fluid-fluid interface to the container wall defines the contact angle, which is the second boundary condition for (4). Through solution of (4), the meniscus height can be expressed as a function of the contact angle. Conversely, upon inverting this relation, the meniscus height determines the contact angle. See Table 1. Equation (4) is solved with omission of the nonlinear term [52]. See Fig. 5.

The weak dependence of the meniscus height on the strongly varying Atwood number suggests that the Atwood number is not the primary driver in the unusual nature of Exp. 114 relative to the others in this series. Rather, we suggest that the difference is a consequence of the significantly reduced pressure in Exp. 114. According to Young's formula [32], the contact angle is
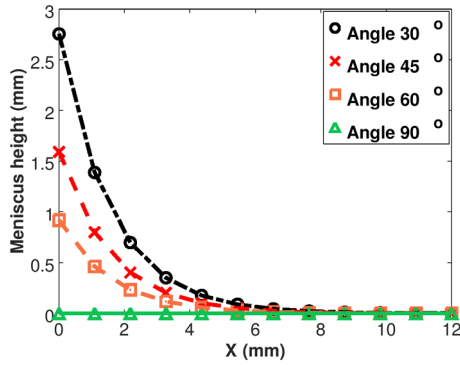
Figure 5: The meniscus profile for contact angles 30°, 45°, 60° and 90°, based on the Atwood number $A = 0.79$ of Exp. 105.

proportional to the difference between the fluid-wall surface tensions on the two sides of the interface. The reduced pressure reduces the wall-gas surface tension and results in a smaller contact angle. The smaller contact angle gives rise to a more rapidly growing edge spike, as can be seen from the steep slope for Exp. 114 in Fig. 6, presumably resulting in a somewhat enlarged meniscus m-bubble and bulk bubble delay. This delay is the striking feature clearly visible in the experimental plates, see Fig. 3, which now has a possible physics based interpretation.

The sign of g changes upon acceleration and becomes some 30 times larger in magnitude according to (4). The resulting new stable meniscus is in the reversed direction, and much larger. However, this reversed stability meniscus does not occur. The Rayleigh-Taylor unstable acceleration of the static meniscus is stronger. As is clear from the experimental plates, the meniscus seeds a single mode Rayleigh-Taylor spike.

3. Instability analysis

The picture indicated in Fig. 4 and its discussion, of acceleration growth rates with delay terms proportional to t is supported by direct analysis of the experimental data from [49]. The experimental plates were digitized and magnified down to a pixel level, so that sub millimeter phenomena were clearly visible. Each of the plates for the five experiments was analyzed independently by two of the authors, and the results were compared and in the few cases of difference, were reconciled.

Uncertainties in the data reading are of three types. We mention first the identification of the location of the bulk bubbles from the data. These are

Table 2: Data for five immiscible experiments, see Table 6 and Fig. 40 of [49]. $\lambda_m = 2\pi(3\sigma/g(\rho_1 - \rho_2))^{1/2}$, is the maximum unstable wave length, and σ is the surface tension

	99	103	104	105	114
α_2 edge bubbles	0.057	0.059	0.068	0.072	0.060
λ_m (mm)	4.0	4.1	4.2	4.5	4.2
g/g_0	17	16	16	15	16
ρ_1 (g/cm^3)	1.0	1.0	0.626	0.626	0.626
ρ_2 (g/cm^3)	0.0742	0.0319	0.0340	0.0739	0.0318
h_2/h_1	> 1.7	> 1.8	1.9	1.5	2.3
A	0.89	0.97	0.57	0.79	0.90

clearest in experiment 114, see Fig. 3, with limited but still useful data from other experiments. This uncertainty is mitigated by the simulations, which independently of the data interpretation, support the main conclusions of the article.

We mention two additional uncertainties. The location of the 95% concentration location, while omitting edge effects, was assessed qualitatively and thus uncertain. The parallax corrections, utilized in [49], were unavailable to us as the report did not contain the camera location. These two uncertainties are mitigated by the fact that their impact is a few percent, whereas the major concern of the analysis is a factor of 2 discrepancy between the experiments and many simulations in the determination of α_2, to be attributed or not to long wave length noise in the initial data. Small corrections do not influence the analysis of major discrepancies. Small corrections, however, do preclude meaningful comparison of small differences depending on experimentally derived quantities. For this reason, our conclusions are qualitative and not quantitative in nature where they depend on small differences in experimental quantities. This limitation on the interpretation of small effects arises in the analysis of the delay for Exp. 105, where we split the unobserved bulk spike amplitude B from the 3rd plate into a fraction f related to the m-bubble size and delay and the fraction $1 - f$ giving the strength of the random surface perturbation. An appeal to 2D simulations to resolve this issue gives qualitative information only (f is near 1) due to dependence on small effects from the observations.

Summary and background information from these experiments is given in Table 2.

Most of the phenomena analyzed are single effects in that they depend on a single parameter and process. This is in contrast to the observed edge bubbles, whose initial conditions are a sum of three distinct three terms, as discussed in Sec. 3.3.

Table 3: Experimentally observed and simulated edge spike data

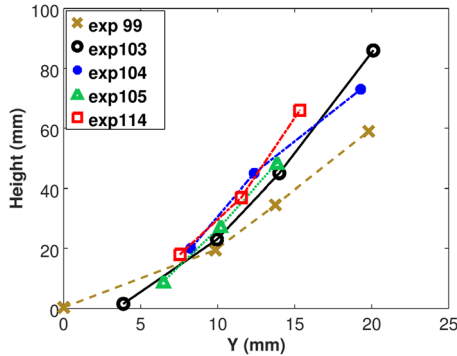|	99	103	104	105	114
exp slope h/Y	4.0	6.2	4.0	5.7	7.6
sim slope h/Y	-	-	-	4.5	-
sim contact angle	-	-	-	34	-
sim meniscus height (mm)				2.4	

Figure 6: Plot of the edge spike penetration distance h_1 vs. the scaled distance $Y = \sqrt{Ag}t$ mm. Data shown for times up to the 4th plate immiscible experiments, data from [49].

3.1. Single effects: edge spikes

The edge spikes are 2D isolated perturbations through Plate 3 and for Exp. 105, through Plate 4, with a translational symmetry along the wall parallel direction. We present experimental data for 5 experiments, Plates 1-4 in Fig. 6 and compare to simulation data for Exp. 105 in Fig. 2, right frame and Table 3. At later times, the effects of the random surface perturbations disrupt the 2D nature of the data. These later times are excluded from our analysis. The Plate 1 data is the initial meniscus, not visible from the experimental plates. Thus the available data is limited to at Plates 2, 3, 4 for Exp. 105 and Plates 2, 3 for the other experiments with approximate validity for Plate 4 in these cases. The edge spike growth for h is approximately linear in time modeled by (3) while they remain 2D. In the simulations, the contact angle is a free parameter. The edge spike slope $v*$ is sensitive to the contact angle, with a smaller contact angle resulting in a steeper slope. Accordingly, we adjust the contact angle to maximize agreements with the experimentally observed slopes $v*$, given by the model (3). We observe from Table 3 that the slopes of the edge bubbles for the two experiments (99 and 104) with no visible bulk bubbles are the smallest, 4.0 mm. The two experiments with marginally visible

Table 4: Experimental bulk growth rate α_2 for immiscible experiments 103, 105, 114 [49] analyzed with the model (2) The miscible experiment 112 is included for comparison, with a nonzero delay. For 112, there are no edge bubbles distinct from bulk bubbles

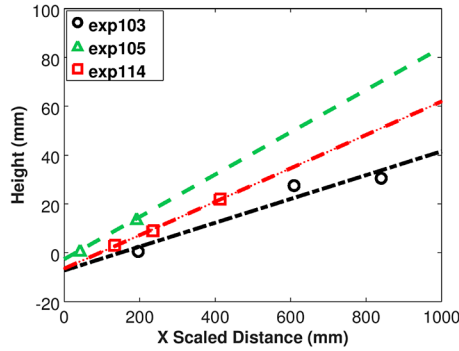|	99	103	104	105	114	112 (misc)
α_2 exp bulk bubble	-	0.049	-	0.087	0.068	0.052
α_2 exp edge bubble	0.057	0.059	0.068	0.072	0.060	0.052
$h_{2,a}$ exp bulk bubble delay (mm)	-	7.3	-	2.7	6.5	4.16
$h_{2,a}$ exp edge bubble delay (mm)	0	0	0	0	0	4.16

Figure 7: Experimental instability growth of bulk bubbles for experiments 103, 105 and 114. The lines through the data are defined by least squares for each of the three experiments. The lines define growth rates which match the observed edge bubble α_2 within about 15%. The final data point for experiment 114 appears to be anomalous and was removed from this analysis.

bulk bubbles have intermediate slopes, 6.2 and 5.7 mm. The single experiment with clearly visible bulk bubbles (114) has the largest edge bubble slope. These trends for the slopes presumably translate into trends in the meniscus height and m-bubble related delay for the bulk bubbles.

3.2. Single effects: bulk bubbles

The bulk bubbles, to the limited extent that they are observable in the data (for several steps of Exps. 103, 105, 114 and isolated steps otherwise), satisfy the steady acceleration law with delay (2), with an acceleration growth rate in agreement to the edge bubble growth rate within an average discrepancy of $\pm 15\%$. Due to the limited data available, the slopes and delay are determined from a least squares fit to data for three experiments. In Table 4 and Fig. 7

Table 5: Comparison of the growth law α_2 and delay for Exp. 105 bubbles. Edge and bulk experimental values are shown (left and right columns) together with simulation growth rates and delays for five values of the fraction f of the $N = 0$ mode assigned to the delay; the fraction $1 - f$ is initialized as broad band initial random perturbations

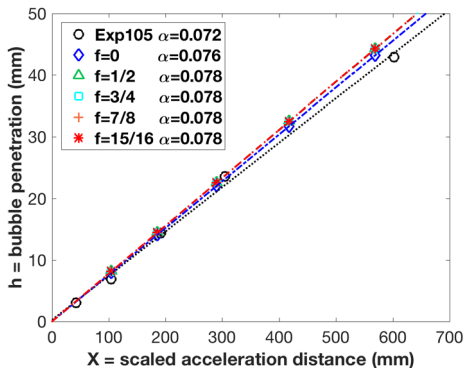|	Exp. edge b.	$N = 0$ $f = 0$	$N = 0$ $f = \frac{1}{2}$	$N = 0$ $f = \frac{3}{4}$	$N = 0$ $f = \frac{7}{8}$	$N = 0$ $f = \frac{15}{16}$	Exp. bulk b.
α_2	0.072	0.076	0.078	0.078	0.078	0.078	0.087
delay (mm)	0.0	0.0	1.23	1.14	1.20	1.21	2.7

Figure 8: Simulation of the bubble growth rate with five values for delay for experiment 105. Experimental data for the edge bubble is also shown.

we present the experimental data that supports these statements.

This data analysis, independently of any simulations, establishes our main point. The experimental and simulated bulk bubbles have a growth rates close to those of the edge bubbles and these growth rates are not affected appreciably by long wave noise in the initial conditions.

Fig. 8 displays simulations of experiment 105 showing that the growth rate α_2 is approximately independent of the size of the delay term, with comparison to experiment summarized in Table 5. We do not model the meniscus explicitly in these simulations. According to the analysis to be presented in Sec. 3.3, we model bulk bubble delays by changes in the initialization for the $N = 0$ mode, split between a constant (fraction f) and broad band initialization (fraction $1 - f$). One curve at the edge of this family ($f = 0$) is the edge bubble simulation [18], already in approximate agreement with experiment [49]. One curve, with f near one, is the bulk bubble. All members of the family share a nearly common α_2, again, confirming our main conclusion: meniscus and edge effects do not appreciably modify the value of α_2,

which is thus not appreciably affected by long wave length noise in the initial conditions.

Commenting on the data in Table 5, we note that the values for α_2 are nearly identical. The experimental bulk bubble value, which has the largest discrepancy, we judge to be the least reliable, due to limited data and the missing parallax correction. The other values are indistinguishable, nearly within the error bounds ± 0.004 proposed for α_2 in [18].

3.3. Combined effects: edge bubbles

We recall the purpose of this paper and its antecedent [18], to show that long wave perturbations of the initial nominally flat interface in the Rayleigh-Taylor instability experiments [49] do not contribute appreciably to the instability growth rate α_2. The effects of the initial perturbations are observed in Plate 3, after they have grown to sufficient size to be visible and while the growth is still in the single mode (exponential growth) regime, so that initial conditions can be reconstructed from this data using analytic formulas. This describes the central enterprise of [18]. Now we insert the effects of the meniscus perturbation to the initial conditions into this analysis. The long wave length perturbations are identified through Fourier analysis of the Plate 3 bubble tips. The bubble tips are in a bounded domain with reflecting boundaries [18], and are discrete, with a spacing on the order of λ_m, the maximally unstable wave length. In this analysis, N is the zero frequency Fourier mode and we interpret $G - N$ as the RMS sum of the nonzero Fourier modes for the bubble tip.

The combined effects problem arises for the analysis of N itself. For such a bounded, discrete Fourier series, the mode $N = 0$ is ambiguous, and can be assigned to either a constant mode or a high wave number mode. This possibility has a physics interpretation, with the constant term, as a fraction f of the $N = 0$ total coming from the meniscus induced m-bubble and contributing to the delay. The high mode number contribution, the fraction $1 - f$, is the broad band noise originating in the bulk bubble random surface perturbations, and contributing to the average bulk bubble position.

Referring to the schematic diagram Fig. 4, the ambiguity arises from the location of B, which our analysis is trying to determine. There are three contributions to the initial conditions of the random surface, of which a single term and the sum N of two others is observed. We identify a splitting of the sum N, to resolve the ambiguity qualitatively. The three components of the initial random surface are the meniscus and its resulting m-bubble and the broad band noise (neither observed) and their (observed) sum N. We resolve

Table 6: The experimental bulk bubble locations and the edge bubble mean and extreme tip locations for the third plate, for five experiments. Units are in mm relative to a centerline $= 0$, and in directions of the negative axis. The G locations experiment are from [49] and are parallax corrected. The B and N data are not parallax corrected. The N locations are from [18] as read from [49]

Plate 3	99	103	104	105	114
B = exp bulk bubble (mm)	5.5	0.5	4.2		3
N = mean bubble tip (mm)	9	9	7.7	6	6.3
G = exp edge bubble (mm)	9	9	11	8	8

this problem through a 2D simulation of the meniscus edge spike and its m-bubble. This fixes the meniscus contact angle. The 2D simulation shows that the random surface initialization as a fraction $1 - f$ of N must be small, but the uncertainties in the reading of observed data preclude going beyond this qualitative conclusion. This qualitative limitation also applies to use of the observed bubble delay from Table 4.

4. Verification and validation of simulations for [49]

4.1. Background

The comprehensive review articles [57, 58] of Zhou set the stage for our shorter and more focused V&V review. As Zhou documents, RT and RM instabilities arise in a wide variety of physical contexts, for which there are natural physical parameters and time scales. Specific applications and specific time regimes encounter a variety of diffusion levels and acceleration rates, sometimes even within a single problem. In this situation, it is clear that a range of experimental programs is advantageous, as is the V&V of their simulation. We focus on low diffusion physics, rapid acceleration and intermediate to moderately late time scales. For short, we refer to this regime as the intermediate asymptotics regime. In this sense the very late time RT asymptotics of [5] is out of our scope. We do not consider single RT mode studies beyond the details where they enter into our main focus.

The intermediate asymptotics regime includes the chaotic flow regime and its transitional development out of random initial conditions, in a context of low diffusion and rapid acceleration physics. Ref. [58] pp. 1-33 provides a summary of the regimes we consider as well as some we do not. Among the important issues identified, we emphasize initial conditions (long wave length dominated or not). A major issue within this regime is the lack of agreement of a number of simulations with data.

4.2. V&V vs. consensus

Verification simulations are contained in [26, 27], validation simulations are summarized in Sec. 4.5.2. A confirming quantitative theory is described in Sec. 4.5.1. The important issue of long wave noise in the initial conditions is addressed [18] with the meniscus and edge effect corrections addressed in the body of this paper.

To emphasize the value of V&V, we recall the first correctly validated RM instability [20, 21], with a new theoretical model of RM growth [54, 55, 56], new experiments removing a controversy regarding initialization with under specified details and two new independent simulations. The result reversed a scientific consensus that poorly characterized initializations were the basis for a disagreement between simulations and experiments. The consensus simulations were in agreement with a theory which was valid for small times. Our analysis showed the theory to be incorrect for times of experimental data collection. There is no possibility of absolute truth in science, but in this example we see that the agreement of theory, experiment and simulation, i.e., V&V, was more reliable than a scientific consensus.

An important standard of science, and one subsumed into V&V methodology, is the duplication of results. This step has already been taken with an independent derivation of a related confirming theoretical model, see Sec. 4.5.1, and with two independent simulations listed below. We also list below 4 additional simulation paths to independent duplication of our results, some rather easily carried out.

1) Duplication and confirmation of the simulation results of Sec. 4.5.2 have already occurred. The simulations [38] based on the front tracking code LEEOR-3D give $\alpha_2 = 0.05$.

2) Duplication and confirmation of simulation has also been achieved, using the Monte Carlo simulation of [4] starting from a random interface. This procedure gives a growth rate $\alpha_2 = 0.052$. There are two other MD simulations in this family of simulations, [3, 23]. These three deal with distinct time periods. [3] deals with the early time, exponentially growing RT phase and contains a self standing V&V effort, with supporting theory and a validating experiment. The second reference deals with late time. Here Zhou notes an anomaly: in late time the RT growth totally stops and the velocity is constant. this calculation and the late time phenomena it predicts is unconfirmed, but in our view it is not necessarily wrong. See Sec. 4.3.

3) To facilitate further independent tests, we have developed FTI, an API for front tracking, to allow ready insertion of this algorithm into other codes [47]. We have implemented FTI for the high energy density code FLASH [33]. See Sec. 4.3.

4) The Lagrangian Particle method [22, 44] has been tested in plasma linear implosion and classical RT problems. This method appears at a glance to be related to smooth particle hydrodynamics (SPH), but is far superior in quality, having removed the instabilities of SPH which constrain it to low orders of accuracy. As the method is particle based, it is well suited to the modeling of low diffusion rapid acceleration physics. Converged LES simulations without recourse to fine DNS grids requires additionally the use of dynamic SGS [15, 34, 31].

5) A simple diagnostic test is to add passive Lagrangian particles to a conventional Eulerian code and observe that it does not track the interface as defined by the Eulerian solver. This test is so simple that it would be surprising if it had not already been taken, but we are not aware of reported results.

6) A conventional Eulerian solver can be used to provide an independent test of low diffusion, rapid acceleration mixing rates. With modern computers, the available resolution is far in excess of what is needed [26] for converged solutions determining α_2 in a low diffusion solver. We propose to use this enhanced computational resource as follows: A conventional solver with artificially lowered resolution will achieve a lower resolution but low diffusion solution. This is accomplished through modified input parameters, namely by adding to the physical viscosity. In this way we treat an augmented physical viscosity as a numerical parameter. An increase in viscosity by a sufficient factor will boost the numerical Schmidt number well above 1, and give an α_2 in the experimental range of values. The result lowers the resolution, but increases the effective Schmidt number of the simulation, defined as the ratio of total (numerical plus physical) viscosity to total (numerical plus physical) concentration diffusion.

4.3. Can $\alpha_2 = 0$?

To state the matter clearly, is it possible that $\alpha_i = 0$ in the late time asymptotic limit with only perturbations in the initial data of a finite, bounded range?

Such a limit, if it occurs, is outside of the range of current experimental observation. Bubble interactions and merger have been observed for the advanced stages of the ablator-plasma interface in NIF [36] and OMEGA [48]

experiments. We discuss $\alpha_2 = 0$ at late times asymptotically as a strictly mathematical possibility. We ask: does the RT t^2 growth rate, observed to agree with experiment for an intermediate time period become zero ($\alpha_2 = 0$) at later times?

The dynamic nature of RT growth, according to the bubble merger model [7], depends on a variation in the bubble radii and velocities at the current (growing with time) length scale defined by the bubble radius. For sustained RT growth, this randomness must have at the current time an amplitude measured as a (small) multiple of the current bubble radius. The required randomness at these large scales is excluded from initial condition perturbations by hypothesis, and so it must be introduced from smaller wave lengths via mode coupling. Such a large scale transfer of randomness requires an inverse cascade of transfer of information from large k values to small. This occurs in 2D turbulence, for length scales longer than those of energy injection, and is excluded in 3D turbulence according to Kolmogorov theory.

4.4. Experiments with low diffusion and rapid acceleration

Within the framework of low diffusion rapid acceleration physics, there are three main classes of experiments to consider: the rocket rig [49], the gas gun [24], and the linear electric motor [10, 43]. Other than [43], the three give comparable acceleration rates α_2, with small variation, which our simulations [26] suggest are due to the differing effects of fluid transport properties between the different experiments. The experiments [43] report somewhat lower values of $\alpha_2 = 0.041$. Comparing the effect of different cutoff concentrations on α_2 from Fig. 2 of [38], we see a 10% drop in α_2 using a 10% cutoff and also a decline with time in the α_2 value. The analyses of ref. [49] truncate some late time data which fall below early time α_2 trend lines. A 10% reduction of the $\alpha_2 = 0.50$ of experiment 102 of [49] gives an α_2 of 0.045, which is nearly consistent with [43]. We do not consider the low diffusion but slow acceleration hot-cold, fresh-salt and air-helium channels of [2, 39, 40] nor the weight and pulley drop tower experiments of [37, 42].

In summary, we have a nearly or fully consistent set of experimental values within the range of physics we consider.

4.5. Growth rate modeling

4.5.1. Theory   Our theory and simulation results are both in agreement with the intermediate asymptotics RT experiments of Sec. 4.4. We originated the bubble merger concepts and model development. According to the bubble merger model, adjacent bubbles, one slightly more advanced than the other,

Table 7: Predictions of the bubble merger model with good agreement to three experiments, for the bubble growth rate α_2 and for related growth rates α_r and α_h for the mean bubble radius and for the mean height separation between leading and training bubbles

Experiment	α_r	$\alpha_r^{\mathbf{exp}}$	α_h	$\alpha_h^{\mathbf{exp}}$	α_2	$\alpha_2^{\exp}$
104	0.014	0.009	0.027	0.028	0.057	0.068
105	0.014	0.012	0.027	0.021	0.056	0.072
114	0.011	0.011	0.022	0.036	0.054	0.060

interact, and the larger, more advanced one speeds up while the slower one drops behind, and falls out of the front defined by the leading bubbles [46, 45]. As this model has evolved, the bubble front motion has two components, one due to the intrinsic motion of the bubbles comprising the front, and the other due to the interaction between slightly displaced neighboring bubbles. Validation of the bubble interaction comes from [19]. The concept of an envelope velocity was introduced in [16]. A statistical version of the model with an RNG fixed point was developed in [17]. This fixed point was evaluated in [53] with the value $\alpha_2 = 0.045$ in approximate agreement with experiment. An important advance [8] uses the bubble merger model to predict α_2 for three experiments. This model also predicts the mean bubble radius and the mean height separation between the most advanced and retarded bubble tips, both characterized with their own α. See Table 7. This circle of ideas has been confirmed in an independent development, [1], although with incorrect predictions of the bubble height to radius ratio and with an extension of the ideas to the modeling of spikes.

This theoretically validated prediction has been extended to the prediction of α_1, based on a closed form expression for α_1/α_2 [7], and including predictions for the dimensionless Richtmyer-Meshkov asymptotics θ_i. The predictions for α_1 show good agreement to the experimental Linear Electric Motor (LEM) data [9, 11].

4.5.2. Simulations   In a series of investigations, we have obtained excellent simulation agreement between theory and experiment, even at the level of finding the differing values of α_2 between experiments due to the fluid transport properties of the experiment [26, 27, 18, 29, 13]. See Table 8.

In contrast, a comprehensive study [12] illustrates the central problem. The experiments show a value $\alpha_2 = 0.057 \pm 0.008$ while the simulations show the lower growth rates $\alpha_2 = 0.025 \pm 003$, less than 50% of the experimental values.

Aside from the discrepancy of the simulations relative to the experiments, there is considerable variation among the distinct simulations reported in [12].

Table 8: Comparison of FT simulation to experiment. *Original simulation results presented here. † Simulation and experimental results reported with two significant digits only. Discrepancy refers to the comparison of results outside of uncertainty intervals, if any, as reported

Ref.	Exp.	Sim. Ref.	$\alpha_{\exp}$	$\alpha_{\sim}$	Discrepancy †
[49]	#112	[26]	0.052	0.055	6%
[49]	#105*	[18]	0.072	0.078 ± 0.004	7%
[49, 41]	10 exp.	[14]	0.055-0.077	0.066	0%
[39]	air-He	[29]	0.065-0.07	0.069	0%
[35]	Hot-cold	[18] [26]	0.070 ± 0.011	0.075	0%
[35]	Salt-fresh	[18]	0.085 ± 0.005	0.084	0%

It has been proposed that under-specified initial conditions are the cause of this disparity. Our simulations indicate that initial condition variation should modify the delay but not the growth rates of the distinct simulations. On this basis, a more plausible explanation lies in the varying levels of fluid transport (effective Schmidt and Prandtl numbers), which should affect the simulation growth rates.

A validation issue newly addressed here is next to leading order large time solution asymptotics. V&V for the next to leading order asymptotics is critical for understanding of immiscible fluids, regarding the influence of a meniscus at the immiscible fluid interface-container boundary triple point. The meniscus is a significant perturbation to the initial conditions, and the boundary layer interface perturbation it generates has a role developed in Sec. 3.

5. Summary

From the introduction, we repeat our main conclusion.

The leading order time asymptotics $\alpha_2 \sim 0.06 \pm 0.01$ for Rayleigh-Taylor mixing observed experimentally [49] is not contaminated appreciably by long wave noise in the initial conditions. The view that long wave length noise in the initial conditions could be an important factor in the asymptotic instability growth rate α for Rayleigh-Taylor mixing was explored in [50], where an adjustable amplitude multiplies the k^{-3} power spectrum (k is a wave number). Modification of this adjustable amplitude in the initial conditions was shown to yield code results that match experimental data.

Our agreement with the experiment in Sec. 3 includes nearly exact matches to distinct experiments with distinct α's. For high-Reynolds experiments in [49], we constructed the initial conditions and found

the initial power spectral power law $k^{-3.3}$ for the reconstructed long wave noise spectrum as well as the amplitude multiplying the power law. Our resulting agreement with experiment is acknowledged in [51]. The [51] compares DNS and ILES simulations which produce a growth rate 0.06 under a variety of assumptions not constrained by reference to experimental data on the initial conditions for moderate Reynolds numbers (< 5000), which may not be relevant to the high-Reynolds experiments.

In support of our central claim, we offer the three secondary conclusions:

a) Adherence to standards of V&V is a more reliable indicator of scientific truth than is a scientific consensus.

b) Multiple independent simulations (free from artifacts of numerical diffusion) and a quantitative theory from multiple independent groups support standards of V&V for our central claim.

c) The role of the meniscus in immiscible experiments is analyzed in detail here, and found to contribute to the growth at a next to leading order in the time asymptotics, but leaves the α_2 leading order asymptotics largely unchanged. Thereby, our central claim, as analyzed in [18], is confirmed.

Concerning item (a), we note that standards for V&V were developed to address the obvious shortcomings of expert opinion and expert judgment.

Item (b) documents our belief that we have met standards of V&V as normally defined. We have established a V&V program for our RT simulations, with simulations showing excellent agreement with experiment and with supporting quantitative theory, also in agreement with experiments. The simulations have been repeated independently by two groups, using two different simulation packages and the theory has been developed and confirmed by two independent groups. We anticipate (and welcome) others to question what we have done. To allow the questioning to proceed constructively, we outline a protocol to allow multiple routes for others to adapt our technology. Within this road, some options are easily followed, and provide a path for others to check independently our main conclusions. Some are so simple that they may have already been taken. We identify two shortcomings in common simulation methods, critical in order to obtain for RT simulations which agree with experimental data.

The detailed contribution of this paper comes under item (c).

The meniscus corrections to our estimate of the influence upon α_2 of the long range noise in the initial conditions were found to be small. The methodology is a combination of data analysis and simulation, connected by a simple theoretical framework. We have a detailed and new reading of the

experimental data. We have detailed 2D simulations of the meniscus induced edge spike for the limited time that the experiments themselves show 2D edge spikes. We simulate the associated m-bubble, which introduces a delay in the growth of the bulk bubbles. We compute bulk bubbles in new 3D simulations with varying degrees of delay, and observe only small effects on the leading asymptotic growth rate α_2. The simple theory is built around the notion of a delay for the onset of the asymptotic regime.

Acknowledgements

References

[1] U. Alon, J. Hecht, D. Ofer, and D. Shvarts. Power laws and similarity of Rayleigh-Taylor and Richtmyer-Meshkov mixing fronts at all density ratios. *Phys. Rev. Lett.*, **74**:534–538, 1995.

[2] A. Banerjee and M. J. Andrews. 3D simulations to investigate initial condition effects on the growth rate of Rayleigh-Taylor mixing. *Int. J. Heat and Mass Transfer*, **52**:3906–3917, 2009.

[3] J. L. Barber, J. Kadau, T. C. Germann, and B. J. Alder. Initial growth of the Rayleigh-Taylor instability via molecular dynamics. *The European Physical Journal B*, **64**:00311, 2008.

[4] J. L. Barber, K. Kadau, T. C. Germann, and B. J. Alder. Atomistic simulation of the Rayleigh-Taylor instability. *Journal of Physics Conference Series*, **46**:58–62, 2006.

[5] W. Cabot and A. Cook. Reynolds number effects on Rayleigh-Taylor instability with possible implications for type Ia supernovae. *Nature Physics*, **2**:562–568, 2006.

[6] B. Cheng, T. J. T. Kwan, Y. M. Wang, S. H. Batha, and F. Wysocki. Effects of preheat and mix on the fuel adiabat of imploding capsules. *Physics of Plasmas*, **23**:120792, 2016.

[7] B. CHENG, J. GLIMM, and D. H. SHARP. Density dependence of Rayleigh-Taylor and Richtmyer-Meshkov mixing fronts. *Phys. Lett. A*, **268**:366–374, 2000.

[8] B. CHENG, J. GLIMM, and D. H. SHARP. A 3-D RNG bubble merger model for Rayleigh-Taylor mixing. *Chaos*, **12**:267–274, 2002. MR1907639

[9] G. DIMONTE. Nonlinear evolution of the Rayleigh-Taylor and Richtmyer-Meshkov instabilities. *Phys. Plasmas*, **6**(5):2009–2015, 1999. MR1701504

[10] G. DIMONTE and M. SCHNEIDER. Turbulent Rayleigh-Taylor instability experiments with variable acceleration. *Phys. Rev. E*, **54**:3740–3743, 1996.

[11] G. DIMONTE and M. SCHNEIDER. Density ratio dependence of Rayleigh-Taylor mixing for sustained and impulsive acceleration histories. *Phys. Fluids*, **12**:304–321, 2000.

[12] G. DIMONTE, D. L. YOUNGS, A. DIMITS, S. WEBER, M. MARINAK, S. WUNSCH, C. GARSI, A. ROBINSON, M. ANDREWS, P. RAMAPRABHU, A. C. CALDER, B. FRYXELL, J. BIELLE, L. DURSI, P. MACNIECE, K. OLSON, P. RICKER, R. ROSNER, F. TIMMES, H. TUBO, Y.-N. YOUNG, and M. ZINGALE. A comparative study of the turbulent Rayleigh-Taylor instability using high-resolution three-dimensional numerical simulations: The Alpha-Group collaboration. *Phys. Fluids*, **16**:1668–1693, 2004.

[13] E. GEORGE and J. GLIMM. Self similarity of Rayleigh-Taylor mixing rates. *Phys. Fluids*, **17**:1–13, 2005. Stony Brook University Preprint SUNYSB-AMS-04-05. MR2147673

[14] E. GEORGE, J. GLIMM, X.-L. LI, Y.-H. LI, and X.-F. LIU. Influence of scale-breaking phenomena on turbulent mixing rates. *Phys. Rev. E*, **73**:016304, 2006. MR2223067

[15] M. GERMANO, U. PIOMELLI, P. MOIN, and W. H. CABOT. A dynamic subgrid scale eddy viscosity model. *Phys. Fluids A*, **3**:1760–1765, 1991.

[16] J. GLIMM, X.-L. LI, R. MENIKOFF, D. H. SHARP, and Q. ZHANG. A numerical study of bubble interactions in Rayleigh-Taylor instability for compressible fluids. *Phys. Fluids A*, **2**(11):2046–2054, 1990. MR1078614

[17] J. GLIMM and D. H. SHARP. Chaotic mixing as a renormalization group fixed point. *Phys. Rev. Lett.*, **64**:2137–2139, 1990. MR1049577

[18] J. Glimm, D. H. Sharp, T. Kaman, and H. Lim. New directions for Rayleigh-Taylor mixing. *Phil. Trans. R. Soc. A*, **371**:20120183, 2013. Los Alamos National Laboratory Preprint LA-UR 11-00423 and Stony Brook University Preprint SUNYSB-AMS-11-01.

[19] J. Glimm and X.-Li. On the validation of the Sharp-Wheeler bubble merger model from experimental and computational data. *Phys. Fluids*, **31**:2077–2085, 1988.

[20] J. W. Grove, R. Holmes, D. H. Sharp, Y. Yang, and Q. Zhang. Quantitative theory of Richtmyer-Meshkov instability. *Phys. Rev. Lett.*, **71**(21):3473–3476, 1993.

[21] R. Holmes, G. Dimonte, B. Fruxell, M. Gittings, J. Grove, M. Schneider, D. Sharp, A. Velkovich, and R. Weaver. Richtmyer-Meshkov instability growth: experiment, simulation and theory. *JFM*, **389**:55–79, 1999. MR1707239

[22] S. C. Hsu, S. J. Langendorf, K. C Yates, J. P. Dunn, S. Brockington, A. Case, E. Cruz, F. D. Witherspoon, M. A. Gilmore, J. T. Cassibry, R. Samulyak, P. Stoltz, K. Schille, W. Shih, K. Beckwith, and Y. C. F. Thio. Experiment to form and characterize a section of a spherically imploding plasma liner. *ArXiv e-prints*, 2017. arXiv:1710.00149.

[23] K. Kadau, J. L. Barber, T. C. Germann, and B. J. Alder. Scaling of atomistic fluid dynamics simulations. *Phys. Rev. E*, **78**:045301, 2008.

[24] Ya. Kucherenko, L. I. Shibarshev, V. I. Chitaikin, S. A. Balabin, and A. P. Palaev. Experimental investigation into the the self-similar mode of the gravitational turbulent mixing. In *Proceedings of the 3rd International Workshop on the Physics Compressible Turbulent Mixing*. 1991.

[25] K. R. Lechin. Memorandum for NNSA's high energy density and inertial confinement fusion community. 2016.

[26] H. Lim, J. Iwerks, J. Glimm, and D. H. Sharp. Nonideal Rayleigh-Taylor mixing. *Proc. Natl. Acad. Sci.*, **107**(29):12786–12792, 2010. Stony Brook University Preprint SUNYSB-AMS-09-05 and Los Alamos National Laboratory Preprint LA-UR 09-06333.

[27] H. Lim, J. Iwerks, Y. Yu, J. Glimm, and D. H. Sharp. Verification and validation of a method for the simulation of turbulent mixing. *Physica Scripta*, **T142**:014014, 2010. Stony Brook University Preprint

SUNYSB-AMS-09-07 and Los Alamos National Laboratory Preprint LA-UR 09-07240.

[28] J. Lindl, O. Landen, J. Edwards, E. Moses, and NIC Team. Review of the national ignition campaign 2009–2012. *Physics of Plasmas*, **21**(2), 2014.

[29] X.-F. Liu, E. George, W. Bo, and J. Glimm. Turbulent mixing with physical mass diffusion. *Phys. Rev. E*, **73**:056301, 2006. MR2242603

[30] E. M. Loberov. Shape and volume of liquid meniscus of the surface of a specimen. *J. Eng. Phys. and Thermodynamics*, **86**:634–644, 2013.

[31] T. Ma. *Large-eddy simulation of variable density flows.* PhD thesis, University of Maryland, 2006.

[32] L. Makkoren. Young's equation revisited. *J. Phys. Condens. Matter*, 28, 2016.

[33] J. Melvin, H. Lim, V. Rana, B. Cheng, J. Glimm, D. H. Sharp, and D. C. Wilson. Sensitivity of inertial confinement fusion hot spot properties to the deuterium-tritium fuel adiabat. *Physics of Plasmas*, **22**:022708, 2015.

[34] P. Moin, K. Squires, W. Cabot, and S. Lee. A dynamic subgrid-scale model for compressible turbulence and scalar transport. *Phys. Fluids A*, **3**:2746–2757, 1991.

[35] N. J. Mueschke. *Experimental and numerical study of molecular mixing dynamics in Rayleigh-Taylor unstable flows.* PhD thesis, Texas A and M University, 2008.

[36] D. A. Martinez, V. A. Smalyuk, J. O. Kane, A. Castner, S. Liberatore, and L. P. Masse. Evidence for a bubble-competition regime in indirectly driven ablative Rayleigh-Taylor experiments on the NIF. *PRL*, **114**(21):215004, 2015.

[37] D. H. Olson and J. W. Jacobs. Experimental study of Rayleigh-Taylor instability with complex initial perturbation. *Phys. Fluids*, 21, 2009.

[38] D. Oron, L. Arazi, D. Kartoon, A. Rikanati, U. Alon, and D. Shvarts. Dimensionality dependence of the Rayleigh-Taylor and Richtmyer-Meshkov instability late-time scaling laws. *Phys. of Plasmas*, **8**:2883–2890, 2001.

[39] P. Ramaprabhu and M. Andrews. Experimental investigation of Rayleigh-Taylor mixing at small atwood numbers. *J. Fluid Mech.*, **502**:233–271, 2004.

[40] P. Ramaprabhu and M. Andrews. On the initialization of Rayleigh-Taylor simulations. *Phys. Fluids*, 16, 2004.

[41] K. I. Read. Experimental investigation of turbulent mixing by Rayleigh-Taylor instability. *Physica D*, **12**:45–58, 1984.

[42] M. S. Roberts and J. W. Jacobs. The effects of forces small-wavelength finite-bandwidth initial perturbations and miscibility on the turbulent Rayleigh-Taylor instability. *J. Fluid Mech.*, **787**:50–83, 2016. MR3482021

[43] Michael Scott Roberts. *Experiments and simulations on the incompressible Rayleigh- instability with small wavv length initial perturbations.* Phd thesis, University of Arizona, 2012.

[44] R. Samulyak, X. Wang, and H.-C. Chen. Lagrangian partilce method for compressible fluid dynamics. *JCP*, **362**:1–19, 2018. MR3774921

[45] D. H. Sharp. An overview of Rayleigh-Taylor instability. *Physica D*, **12**:3–18, 1984.

[46] D. H. Sharp and J. A. Wheeler. Late stage of Rayleigh-Taylor instability. Technical report, Institute of Defense Analyses, 1961. Unpublished Technical Report.

[47] D. She, R. Kaufman, H. Lim, J. Melvin, A. Hsu, and J. Glimm. Front-tracking methods. In *Handbook of Numerical Methods for Hyperbolic Problems, volume 17*, pages 383–402. Elsevier, 2016. MR3643835

[48] V. A. Smalyuk, O. Sadot, J. A. Delettrez, D. D. Meyerhofer, S. P. Regan, and T. C. Sangster. Fourier-space nonlinlear Rayleigh-Taylor growth measurments of 3d laser-imprinted modulations in planar targets. *PRL*, **95**:215001, 2005.

[49] V. S. Smeeton and D. L. Youngs. Experimental investigation of turbulent mixing by Rayleigh-Taylor instability (part 3). AWE Report Number 0 35/87, 1987. MR1024395

[50] D. L. Youngs. The density ratio dependence of self-similar Rayleigh-Taylor mixing. *Phil. Trans. R. Soc. A*, **371**:20120173, 2013. MR3123294

[51] D. L. Youngs. Rayleigh-Taylor mixing: direct numerical simulation and implicit large eddy simulation. *Phys. Scr.*, **92**:074006, 2017.

[52] H. Zhang. PhD thesis, Stony Brook University, 2018.

[53] Q. Zhang. Validation of the chaotic mixing renormalization group fixed point. *Phys. Lett. A*, **151**:18–22, 1990. MR1085169

[54] Q. Zhang and S. Sohn. An analytical nonlinear theory of Richtmyer-Meshkov instability. *Phys. Lett. A*, **212**:149–155, 1996. MR1378608

[55] Q. Zhang and S. Sohn. Nonlinear theory of unstable fluid mixing driven by shock waves. *Phys. Fluids*, **9**:1106–1124, 1997. MR1437567

[56] Q. Zhang and S. Sohn. Quantitative theory of Richtmyer-Meshkov instability in three dimensions. *Zeit. angew. Math. Phys.*, **50**:1–46, 1999. MR1674197

[57] Y. Zhou. Rayleigh-Taylor and Richtmyer-Meshkov instability induced flow, turbulence, and mixing, i. *Physics Reports*, **720–722**:1–136, 2017. MR3735086

[58] Y. Zhou. Rayleigh-Taylor and Richtmyer-Meshkov instability induced flow, turbulence, and mixing, ii. *Physics Reports*, **723–725**:1–160, 2017. MR3735087

[59] Y. Zhou, N. Ray, H. Lim, S. Wang, V. F. de Almeida, J. Glimm, X.-L. Li, and X. Jiao. Development of a front tracking method for two-phase micromixing of incompressible viscous fluids with interfacial tension in solvent extraction. Technical Report ORNL/TM-2012/28, Oak Ridge National Laboratory, 2012.

H. Zhang
Department of Applied Mathematics and Statistics
Stony Brook University
Stony Brook, NY 11794-3600
USA
E-mail: hbcbh1999@gmail.com

T. Kaman
Department of Mathematical Sciences
University of Arkansas
Fayetteville, AR 72701
USA
E-mail: tkaman@uark.edu

D. She
Department of Applied Mathematics and Statistics
Stony Brook University
Stony Brook, NY 11794-3600
USA
E-mail: sxhedan@gmail.com

B. Cheng
Los Alamos National Laboratory
NM 87545
USA
E-mail: bcheng@lanl.gov

J. Glimm
Department of Applied Mathematics and Statistics
Stony Brook University
Stony Brook, NY 11794-3600
USA
E-mail: james.glimm@stonybrook.edu

D. H. Sharp
Los Alamos National Laboratory
NM 87545
USA
E-mail: dcso@lanl.gov